Signed Lp-distance fields

Signed L_p-distance Fields

Alexander Belyaev [a] Pierre-Alain Fayolle [b] Alexander Pasko [c]

[a] School of Engineering & Physical Sciences, Heriot-Watt University, Edinburgh, UK
[b] Computer Graphics Laboratory, University of Aizu, Japan
[c] The National Centre for Computer Animation, Bournemouth University, UK

Abstract

We introduce and study a family of generalized double-layer potentials which are used to build smooth and accurate approximants for the signed distance function. Given a surface, the value of an approximant at a given point is a power mean of distances from the point to the surface points parameterized by the angle they are viewed from the given point. We analyze mathematical properties of the potentials and corresponding approximants. In particular, approximation accuracy estimates are derived. Our theoretical results are supported by numerical experiments which reveal high practical potential of our approach.

Key words: approximate distance functions, singular integrals, generalized double potentials

1. Introduction

Singular integrals are central to many mathematical and physical theories and constructions. In this paper, we use singular integrals to construct smooth approximations of distance functions. The paper is inspired by recent works [15,8,4] where remarkable properties of the mean value normalization function (the sum of the mean value weights in the case of a polygon/polyhedron) were discovered and studied. We introduce signed L_p-distance fields, simple but useful generalizations of the mean value normalization function, and exploit their properties to build smooth approximations to the signed distance function.

For many applications, the exact distance field is not needed and smooth approximations of the distance field are employed. For example, in the area of solid modeling, Shapiro and co-workers [2,27] discussed Ricci operations [24] and used R-functions [26] for building approximate distance fields from local approximations.

Fayolle et al. [10] developed smooth alternatives to the classical min/max operations for constructing signed approximate distance functions. Very recently, Freytag et al. [12] introduced sampled smooth approximations of a distance function and used them to enhance the Kantorovich method [17,18] for computational mechanics purposes. In image processing and computer graphics, Ahuja, Chuang, and co-workers [1,6] and Peng et al. [22,23] introduced generalized potential fields and applied them for shape skeletonisation and 3D texture modeling, respectively. It is also worth to mention very recent works [14,7] where the distance function and geodesics are approximated by solutions of certain partial differential equations.

Our approach is conceptually close to that of Ahuja and Chuang (and, therefore, to that of Peng et al. who re-introduced Ahuja-Chuang ideas for computer graphics applications) but instead of using generalized Newtonian potentials we introduce and study a family of generalized double-layer potentials and corresponding signed L_p-distance fields.

There are several advantages of using generalized double-layer potentials to compare with their single-layer counterparts. In particular,

(i) our signed L_p-distance fields deliver smooth and accurate approximations of the signed distance function;
(ii) exact formulas for the generalized double-layer potentials generated by triangle meshes (polylines in 2D) can be obtained;
(iii) mathematical properties of the generalized double-layer potentials and their corresponding signed L_p-distance fields are easy to analyze;
(iv) our generalized double-layer potentials can be considered as a generalization of the mean value normalization function [8,4] and can be used for high-order transfinite interpolation purposes.

It is interesting that singular integrals similar to the double-layer potentials we deal with serve as a main building block for the so-called *surface generalized Born model* in biomolecular modeling [13,25].

The purpose of this paper is to provide the reader with insights into mathematical properties of L_p-distance fields and reveal their high potential for various applications.

2. Generalized double-layer potentials

Consider a smooth oriented hyper-surface $S \subset \mathbb{R}^n$ and a singular integral

$$\phi_p(\boldsymbol{x}) = \int_S \frac{\boldsymbol{n}_y \cdot (\boldsymbol{y}-\boldsymbol{x})}{|\boldsymbol{x}-\boldsymbol{y}|^{n+p}} \sigma(\boldsymbol{y})\, dS_y, \quad p \geq 0, \tag{1}$$

where $\boldsymbol{x}$ is a point outside S, $\boldsymbol{y} \in S$, $\boldsymbol{n}_y$ is the orientation normal at $\boldsymbol{y}$, dS_y is the surface element at $\boldsymbol{y}$, and $\sigma(\boldsymbol{y})$ is a density function defined on S. The classical double-layer potential corresponds to (1) with $p = 0$. If the electric dipoles are distributed over S with density σ, then $\phi_0(\boldsymbol{x})$ is proportional to the electric field generated by the dipoles at $\boldsymbol{x}$.

Let us assume that $\sigma \equiv 1$ (i.e., the dipoles are uniformly distributed over S) and introduce a generalized double-layer potential by

$$\varphi_p(\boldsymbol{x}) = \int_S \frac{\boldsymbol{n}_y \cdot (\boldsymbol{y}-\boldsymbol{x})}{|\boldsymbol{x}-\boldsymbol{y}|^{n+p}} dS_y = \int_\Omega \frac{d\Omega_y}{|\boldsymbol{x}-\boldsymbol{y}|^p}, \tag{2}$$

where $p > 0$, Ω is the unit sphere centered at $\boldsymbol{x}$, and $d\Omega_y$ is the solid angle at which surface element dS_y is seen from $\boldsymbol{x}$. We have used a simple relation

$$dS_y = \rho^n d\Omega_y / \, h \text{ with } \rho = |\boldsymbol{x}-\boldsymbol{y}| \text{ and } h = \boldsymbol{n}_y \, (\boldsymbol{y}-\boldsymbol{x}) \, .$$

Here h is the distance from $\boldsymbol{x}$ to the plane tangent to S at $\boldsymbol{y}$. The two-dimensional analog of (2) can be written in polar coordinates as

$$\varphi_p(\boldsymbol{x}) = \int_0^{2\pi} \frac{d\theta}{\rho(\theta)^p}, \tag{3}$$

where θ is the angle between vector $\boldsymbol{y}-\boldsymbol{x}$ and a fixed direction.

Note that the surface integral in (2) is correctly defined for an arbitrary smooth oriented surface S, while the integral over unit sphere Ω is properly defined if domain D is star-shaped w.r.t. $\boldsymbol{x}$. In order to drop this limitation for the integral over Ω we follow a standard approach of alternating signs (see, for example, [8,4]). Consider a ray originated at $\boldsymbol{x}$ and intersecting S in m points $\boldsymbol{y}_1, \ldots, \boldsymbol{y}_m$. We set $\varepsilon_i = 1$ if the ray $[\boldsymbol{x}, \boldsymbol{y}_i)$ arrives at $\boldsymbol{y}_i$ from positive side of S, $\varepsilon_i = -1$ if the ray approaches $\boldsymbol{y}_i$ from negative side of S, and $\varepsilon_i = 0$ if the ray is tangent to S at $\boldsymbol{y}_i$. Now let us assume that $|\boldsymbol{x}-\boldsymbol{y}|^p$ in the denominator of the integral over Ω in (2) means $\sum_i \varepsilon_i \, |\boldsymbol{x}-\boldsymbol{y}_i|^p$. See the left and middle images of Fig. 1 below for a visual explanation.

If S is a closed curve and $p = 1$ then (3) defines the normalization function corresponding to the transfinite mean value interpolation for the domain bounded by S. It is easy to see that

$$\psi_p(\boldsymbol{x}) = \left[1 \,/ \varphi_p(\boldsymbol{x})\right]^{1/p}, \quad p \geq 1, \tag{4}$$

vanishes as $\boldsymbol{x}$ approaches S.

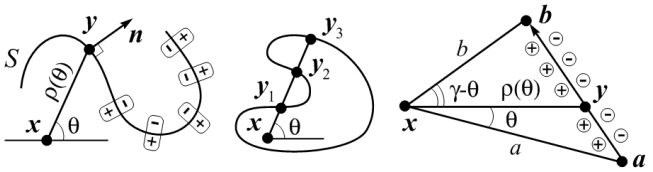

Fig. 1. Left and middle: illustrations for the definition of $\varphi_k(\boldsymbol{x})$. Right: potential $\varphi_k(\boldsymbol{x})$ generated by a segment $\boldsymbol{ab}$ and notations used.

3. Mathematical properties

In this section we formulate our main mathematical results which describe approximation properties of (4). See Appendix A for proofs.

Denote by v_n and a_n the volume of the unit ball in $\mathbb{R}^n$ and the area of the unit sphere, respectively. We have $a_n = n v_n$, $v_0 = 1$, $v_1 = 2$, $v_2 = \pi$, $v_3 = 4\pi/3$, and $a_n = 2\pi^{n/2} \big/ \Gamma(n/2)$, where $\Gamma(\cdot)$ is the Gamma function.

Let D be a domain in $\mathbb{R}^n$ bounded by a piecewise-smooth surface S. Consider a family of functions $d_{\boldsymbol{x}}(\boldsymbol{y}) = \|\boldsymbol{x}-\boldsymbol{y}\|$, $\boldsymbol{y} \in S$, defined on S and parameterized by $\boldsymbol{x} \in D$.

Proposition 1 We always have $\psi_p(\boldsymbol{x}) \to \operatorname{dist}(\boldsymbol{x})$, as $p \to \infty$. In other words, $\psi_\infty(\boldsymbol{x}) = \operatorname{dist}(\boldsymbol{x})$.
If $d_{\boldsymbol{x}}(\boldsymbol{y})$ has continuous second-order partial derivatives in a small vicinity of its global minimum, then

$$\psi_p(\boldsymbol{x}) = \operatorname{dist}(\boldsymbol{x}) \left[1 + \frac{n-1}{2} \frac{\ln p}{p}\right] + O\left(\frac{1}{p}\right), \text{ as } p \to \infty. \tag{5}$$

If D is star-shaped w.r.t. $\boldsymbol{x}$ and $1 < p < q < \infty$, then

$$a_n \psi_1(\boldsymbol{x}) > (a_n)^{1/p} \, \psi_p(\boldsymbol{x}) > (a_n)^{1/q} \, \psi_q(\boldsymbol{x}) > \operatorname{dist}(\boldsymbol{x}).$$

Note that typically the distance-function $d_{\boldsymbol{x}}(\boldsymbol{y})$ is sufficiently smooth in a small neighborhood of its global minimum and, therefore, (5) is valid. A loss of differentiability of $d_{\boldsymbol{x}}(\boldsymbol{y})$ happens when $\boldsymbol{x}$ is sufficiently close to a concave singularity (concave corner, concave edge, etc.) of S.

Although (5) is not fast, below we will see that, after a proper normalization, $\psi_p(\boldsymbol{x})$ delivers a very accurate approximation of $\operatorname{dist}(\boldsymbol{x})$ near S even for small p. Fig. 2 illustrates that in the simplest case of $n = 1$. As seen in the left image, $(a_n)^{1/p} \, \psi_p(\boldsymbol{x})$ converges to $\operatorname{dist}(\boldsymbol{x})$ from above as $p \to \infty$. However a different normalization of $\psi_p(\boldsymbol{x})$ (no normalization is needed if $n = 1$) allows us to obtain a much better approximation $\operatorname{dist}(\boldsymbol{x})$ near the boundary.

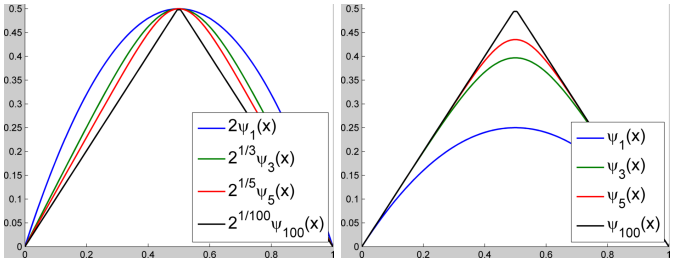

Fig. 2. Approximate distance functions $(a_n)^{1/p} \, \psi_p(\boldsymbol{x})$ (left) and $\psi_p(\boldsymbol{x})$ (right) defined for $[0, 1]$ ($n = 1$). See the main text for details.

Let us introduce the following sequence:

$$c_0 = a_n/2, \quad c_1 = v_{n-1}, \quad c_{p+2} = \frac{p+1}{p+n}\, c_p \tag{6}$$

and define

$$\Psi_p(\boldsymbol{x}) = [c_p]^{1/p}\, \psi_p(\boldsymbol{x}) = [\varphi_p(\boldsymbol{x})/c_p]^{-1/p}.$$

Proposition 2 Let $\boldsymbol{n}$ be the outer normal for $S = \partial D$. If $\boldsymbol{x} \in \partial D$ then

$$\Psi_p(\boldsymbol{x}) = 0, \quad \partial \Psi_p(\boldsymbol{x}) / \partial \boldsymbol{n} = -1.$$

If ∂D contains a planar part and $\boldsymbol{x}$ is an internal point of that planar part, then, in addition,

$$\partial^s \Psi_p(\boldsymbol{x}) / \partial \boldsymbol{n}^s = 0, \quad s = 2, 3, \ldots, p.$$

A simple asymptotic analysis of (6) yields

$$[c_p]^{1/p} = 1 - \frac{n-1}{2}\frac{\ln p}{p} + O\left(\frac{1}{p}\right), \text{ as } p \to \infty,$$

which, in view of the last statement of Proposition 1, gives

$$\Psi_p(\boldsymbol{x}) = \operatorname{dist}(\boldsymbol{x}) + O\left(1/p\right), \text{ as } p \to \infty. \tag{7}$$

Note that, according to Proposition 2, if $\boldsymbol{x}$ is near a flat part of ∂D, $\Psi_p(\boldsymbol{x})$ converges to $\operatorname{dist}(\boldsymbol{x})$ much faster than (7).

Our last theoretical result is presented below. In particular, it implies that the shapes of the graphs of $\psi_p(\boldsymbol{x})$ and $\Psi_p(\boldsymbol{x})$ are similar to that of $\operatorname{dist}(\boldsymbol{x})$.

Proposition 3 We have

$$\Delta \varphi_p(\boldsymbol{x}) = p(p+n)\varphi_{p+2}(\boldsymbol{x})$$

and, therefore, $\psi_p(\boldsymbol{x})$ has no local minima inside D.

Note that the gradient and the other derivatives of $\varphi_p(\boldsymbol{x})$ can be easily obtained by differentiating (2) by $\boldsymbol{x}$ as many times as needed.

4. Singular potentials for polylines and meshes

Let us start from the 2D case and consider the generalized double-layer potentials generated by oriented segment $\boldsymbol{ab}$. Given point $\boldsymbol{x}$, $\gamma = \gamma(\boldsymbol{x})$ is the angle between $\boldsymbol{xa}$ and $\boldsymbol{xb}$, where a and b are the distances from $\boldsymbol{x}$ to $\boldsymbol{a}$ and $\boldsymbol{b}$, respectively, and $\rho(\theta)$ is the distance from $\boldsymbol{x}$ to point $\boldsymbol{y} \in \boldsymbol{ab}$. See the right image of Fig. 1 for a visual illustration of the notations used.

The area of $\triangle \boldsymbol{xab}$ is equal to the sum of areas of $\triangle \boldsymbol{xay}$ and $\triangle \boldsymbol{xyb}$. We have

$$ab \sin\gamma = a\rho(\theta)\sin\theta + b\rho(\theta)\sin(\gamma - \theta),$$

which gives an explicit expression of $\rho(\theta)$

$$\rho(\theta) = \frac{ab\sin\gamma}{a\sin\theta + b\sin(\gamma-\theta)}.$$

Then the generalized double-layer potential $\varphi_p(\boldsymbol{x})$ generated by the segment is given by

$$\varphi_p(\boldsymbol{x}) = \int_0^\gamma \frac{d\theta}{\rho(\theta)^p} = \frac{1}{(ab\sin\gamma)^p}\int_0^\gamma (a\sin\theta + b\sin(\gamma-\theta))^p d\theta.$$

For an arbitrary positive integer p, the value of this integral can be evaluated symbolically (for example, one can use Maple or Mathematica for that). If p is odd, the integral can be expressed as a polynomial of degree p of the variable t, where $t = \tan(\gamma/2)$. In particular,

$$\varphi_1(\boldsymbol{x}) = \left[\frac{1}{a} + \frac{1}{b}\right] t, \quad \varphi_3(\boldsymbol{x}) = \frac{t}{3}\left[\frac{1}{a^3} + \frac{1}{b^3}\right] + \frac{t+t^3}{6}\left[\frac{1}{a} + \frac{1}{b}\right]^3.$$

Note that $\varphi_1(\boldsymbol{x})$ is the weight corresponding to $\boldsymbol{ab}$ and induced by the mean value coordinates [11,15].

If p is even, then more complex expressions are obtained for $\varphi_p(\boldsymbol{x})$, except the case when $p = 0$: $\varphi_0(\boldsymbol{x}) = \gamma(\boldsymbol{x})$ is the standard double-layer potential induced by $\boldsymbol{ab}$.

As expected, in the 3D case, the situation is more complex. Let S be a triangulated surface and $\boldsymbol{abc} \in S$ be a mesh triangle. While $\varphi_0(\boldsymbol{x})$ is just a solid angle at which $\boldsymbol{abc}$ is seen from $\boldsymbol{x}$ and the formula for $\varphi_1(\boldsymbol{x})$ generated by the triangle $\boldsymbol{abc}$ is presented in [16], deriving a closed-form expression for $\varphi_p(\boldsymbol{x})$, $p > 1$ is a difficult and tedious task. Fortunately, a clear way to obtain analytical expressions for a family of singular integrals including $\varphi_p(\boldsymbol{x})$ was proposed very recently in [5].

Given a polyline in 2D (triangle mesh in 3D), the potential $\varphi_p(\boldsymbol{x})$ at point $\boldsymbol{x}$ is obtained by summing the contributions of the polyline segments (mesh triangles).

5. Numerical experiments

In Fig. 3, we provide the reader with a visual comparison of the level sets of $\operatorname{dist}(\boldsymbol{x})$ with those of Ψ_1, Ψ_3 and Ψ_5 for sufficiently complex planar polylines. We observe that the approximation quality improves quickly as k increases.

Fig. 4 visualizes the relative error between $\operatorname{dist}(\boldsymbol{x})$ and $\psi_p(\boldsymbol{x})$ and between $\operatorname{dist}(\boldsymbol{x})$ and $\Psi_p(\boldsymbol{x})$ (normalized L_p-distance), $p = 1, 3, 5$, for a squared domain. As before, the error goes down quickly as p increases. One can observe that the approximation error is relatively high near the corners.

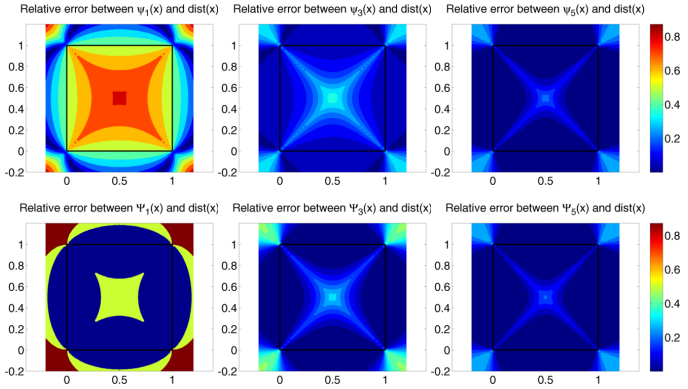

Fig. 4. Estimating the distance function inside and outside a unit square. The first row corresponds to the relative error between the exact signed distance and ψ_1, ψ_3 and ψ_5 respectively. The second row uses the normalized functions: Ψ_1, Ψ_3 and Ψ_5 instead.

In Fig. 5, we investigate the approximation properties of L_p-distance fields near a corner (as before, we calculate the

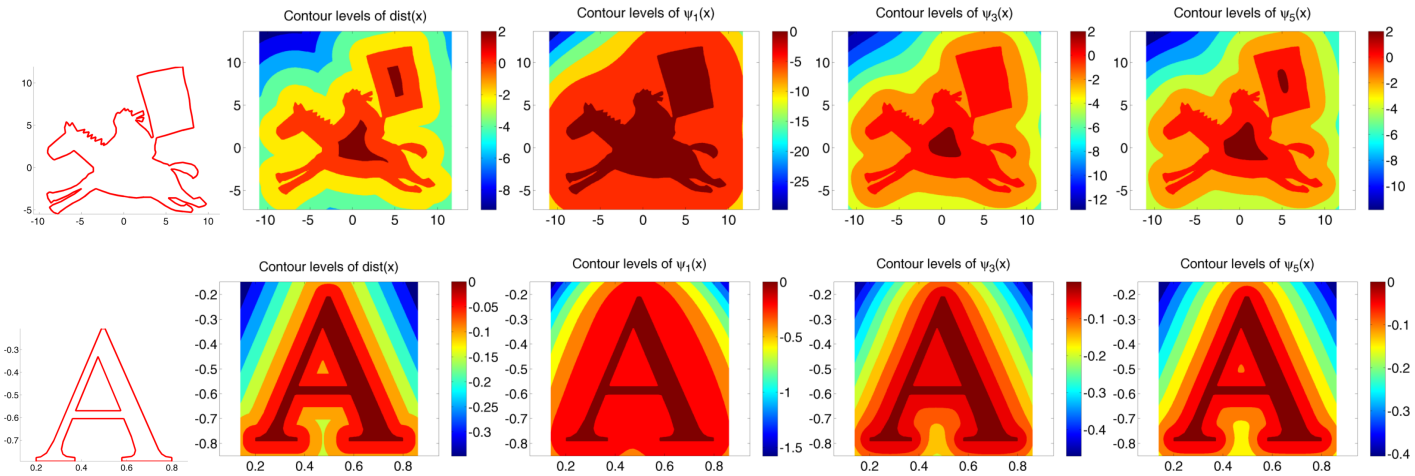

Fig. 3. Polygon approximations of two shapes used in our experiments (left-most images). The polylines consist of 201 and 29 segments respectively. Contour plots for: the signed distance, Ψ_1, Ψ_3 and Ψ_5 for a 2D polyline (columns 2 to 5). Ψ_5 (right-most images) provides already a good approximation of the distance function (second column). Note that the hole for the letter A is properly handled.

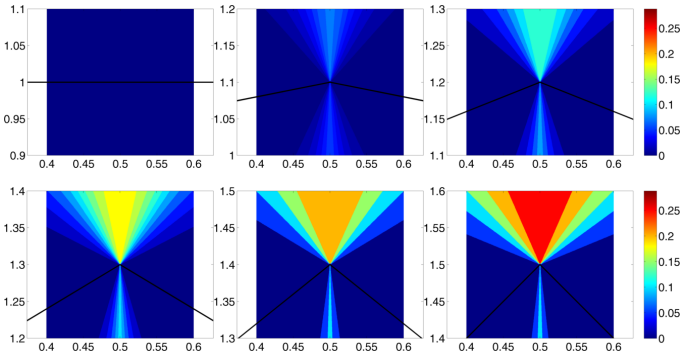

Fig. 5. Relative errors between the exact signed distance and Ψ_5 for various opening angles between two segments. The angles vary between 0° (top row, left column) and 45° (bottom row, right column).

relative error). As expected, the approximation accuracy in a small vicinity of a corner point is lower than it is near an internal point of the segment. Further, the relative error increases on the reflex side of the angle, as the angle becomes sharper. However, even for a sharp corner, the approximation accuracy quickly improves, as k increases. Finally, Fig. 6 illustrates our approach in 3D with the relative error between $\mathrm{dist}(\boldsymbol{x})$ and $\Psi_2(\boldsymbol{x})$ plotted on cross-sections of 3D objects.

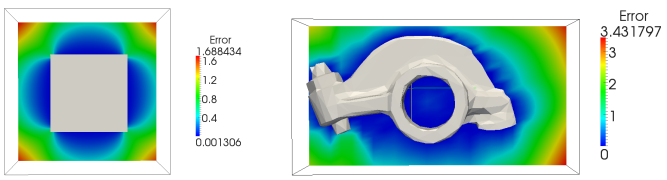

Fig. 6. Relative errors between $\mathrm{dist}(\boldsymbol{x})$ and $\Psi_2(\boldsymbol{x})$ for a cube (left) and the rocker-arm model (right).

6. Discussion and conclusion

In this paper, we have introduced a family of generalized double-layer potentials and their corresponding L_p-distance fields. They possess interesting mathematical properties, and, in particular, the L_p-distance fields deliver smooth and accurate approximations of the distance function.

A practical computation of L_p-distance fields can be accelerated by using a hierarchical approach similar to that developed in [9]. Another possibility is to approximate potentials via fast multipole expansions [19].

The ability of L_p-distance fields to deliver accurate approximations of the distance function not only near the boundary of the object but also deep inside the object (a task which R-functions do not handle well, as demonstreated in [10]) makes them potentially useful for heterogeneous object modeling [3,10].

We also foresee potential applications of the L_p-distance fields in computational mechanics where some new promising computational techniques rely on constructing accurate and efficient approximate smoothed distance functions and their derivatives [12, Section 3.2].

Acknowledgements. We would like to thank the anonymous reviewers of this paper for their valuable and constructive comments.

Appendix A

Proof sketch for Proposition 1. Let $\boldsymbol{x} \in D$ is fixed, Ω is the unit sphere centered at $\boldsymbol{x}$, and $k \to \infty$. We have according to Laplace's method [28, Chapter IX, § 5]

$$\varphi_k(\boldsymbol{x}) = \int_\Omega \frac{d\Omega}{\rho^k} = \int_\Omega \exp\left\{k \ln \frac{1}{\rho}\right\} d\Omega = \frac{C_1 + o(1)}{k^{(n-1)/2}} \frac{1}{\rho_{\min}^k},$$

where $\rho_{\min} = \mathrm{dist}(\boldsymbol{x})$. Thus

$$\psi_k(\boldsymbol{x}) = \left[\frac{1}{\varphi_k(\boldsymbol{x})}\right]^{1/k} = \mathrm{dist}(\boldsymbol{x}) \left[\frac{k^{(n-1)/2}}{C_1 + o(1)}\right]^{1/k}$$

$$= \mathrm{dist}(\boldsymbol{x}) \left[C_2 + o(1)\right]^{1/k} \left(k^{1/k}\right)^{(n-1)/2}, \text{ as } k \to \infty,$$

where C_1 and C_2 are positive constants. It remains to note that, as $k \to \infty$,

$$\left(k^{1/k}\right)^{\frac{n-1}{2}} = \exp\left\{\frac{(n-1)\ln k}{2k}\right\} = 1 + \frac{n-1}{2}\frac{\ln k}{k} + O\left(\frac{1}{k}\right).$$

Above, we assumed that $d_{\boldsymbol{x}}(\boldsymbol{y}) = \rho = \|\boldsymbol{x} - \boldsymbol{y}\|$ has continuous second-order partial derivatives in a small vicinity of its global minimum. This may be not true if $\boldsymbol{x} \in D$ is located near a reflex singularity (e.g., a reflex angle or edge) of $S = \partial D$ and the minimum of $d_{\boldsymbol{x}}(\boldsymbol{y})$ is achieved for $\boldsymbol{y}$ situated on that singularity. In that case, weaker asymptotics can be derived [21] (see also [20, Theorem 2.1]). However convergence $\psi_k(\boldsymbol{x}) \to \operatorname{dist}(\boldsymbol{x})$, as $k \to \infty$, remains true.

Now let us assume that D is star-shaped w.r.t. $\boldsymbol{x} \in D$. An integral version of Jensen's inequality states that

$$F\left[\frac{1}{\mu(R)}\int_R f(\boldsymbol{y})\,d\mu(\boldsymbol{y})\right] \le \frac{1}{\mu(R)}\int_R F\left[f(\boldsymbol{y})\right]\,d\mu(\boldsymbol{y}),$$

where R is a measurable set with finite positive measure μ and $F(t)$ is a convex function. Let $1 < p < q < \infty$, $F(t) = t^{q/p}$, $R = \Omega$ be the unit sphere in $\mathbb{R}^n$, and $f(\boldsymbol{y}) = (1/\rho)^p$, where $\rho = \|\boldsymbol{x} - \boldsymbol{y}\|$. Since $F(t)$ is strictly convex, we have

$$\left[\frac{1}{a_n}\int_\Omega \frac{d\Omega_y}{\rho^{\,p}}\right]^{\frac{1}{p}} < \left[\frac{1}{a_n}\int_\Omega \frac{d\Omega_y}{\rho^{\,q}}\right]^{\frac{1}{q}}, \quad [a_n]^{\frac{1}{p}}\,\psi_p(\boldsymbol{x}) > [a_n]^{\frac{1}{q}}\,\psi_q(\boldsymbol{x}).$$

Proof sketch for Proposition 2. First let us consider the 2D case and study an asymptotic behavior of potential $\varphi_1(\boldsymbol{x})$ generated by a single segment $\boldsymbol{ab}$. See the left image of Fig. 7 for notations used. Assume that h, the distance from $\boldsymbol{x}$ to $\boldsymbol{ab}$, is small: $h \ll 1$. We have $\gamma = \pi - \alpha - \beta$,

$$a(h) = a + O(h^2), \quad \alpha = \arctan\left(h/a\right) = h/a + O(h^2),$$
$$b(h) = b + O(h^2), \quad \beta = \arctan\left(h/b\right) = h/b + O(h^2),$$
$$\tan\frac{\gamma}{2} = \frac{2ab}{a+b}\frac{1}{h} + O(h), \quad \varphi_1(\boldsymbol{x}) = \frac{2}{h} + O(h).$$

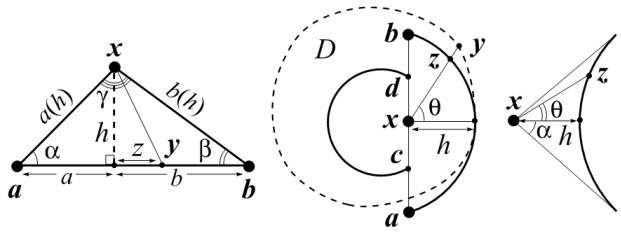

Fig. 7. Notations used for asymptotic analysis of potentials $\varphi_k(\boldsymbol{x})$ generated by a segment (left) and convex and concave circular arcs (middle and right, respectively).

In the 2D case, for a single straight segment, we have

$$\varphi_k(\boldsymbol{x}) = \int \frac{d\theta}{\rho(\theta)^k} = \int \frac{h\,ds_y}{\rho(\theta)^{k+2}}, \quad \rho = |\boldsymbol{x} - \boldsymbol{y}|.$$

Note that

$$\rho = \sqrt{h^2 + z^2}, \quad \frac{\partial\rho}{\partial h} = \frac{h}{\rho}, \quad \frac{\partial}{\partial h}\left(\frac{1}{\rho^{k+2}}\right) = -\frac{(k+2)h}{\rho^{k+4}},$$
$$\frac{\partial}{\partial h}\left(\frac{h}{\rho^{k+2}}\right) = \frac{1}{\rho^{k+2}} - \frac{(k+2)h^2}{\rho^{k+4}}$$

(see the left image of Fig. 7 for the notations used). Thus

$$(k+2)\varphi_{k+2} = \frac{1}{h^2}\varphi_k - \frac{1}{h}\frac{\partial\varphi_k}{\partial h}. \tag{8}$$

Note that $\varphi_k(\boldsymbol{x})$ is odd w.r.t. h. Thus the expansion of $\varphi_k(\boldsymbol{x})$ w.r.t. $h \ll 1$ contains only odd degrees of h. For example,

$$\varphi_1(\boldsymbol{x}) = 2h^{-1} + a_1 h + a_3 h^3 + a_5 h^5 + O\left(h^7\right), \quad h \to 0.$$

Then (8) implies that

$$3\varphi_3(\boldsymbol{x}) = 4h^{-3} - 2a_3 h - 4a_5 h^3 + O\left(h^5\right).$$

One can observe that the right-hand side of (8) kills the linear w.r.t. h term in the expansion of $\varphi_k(\boldsymbol{x})$ and, therefore, the expansion of $\varphi_{k+2}(\boldsymbol{x})$ w.r.t. h contains only one growing term. Mathematical induction yields

$$\varphi_k(\boldsymbol{x}) = c_k\,/h^k + O(h)$$

with c_k defined by (6), where singular potential $\varphi_k(\boldsymbol{x})$ is generated by segment $\boldsymbol{ab}$ and $\boldsymbol{x}$ approaches an internal point of $\boldsymbol{ab}$. For the potential generated by a polygon containing segment $\boldsymbol{ab}$, we have a slightly bigger remainder:

$$\varphi_k(\boldsymbol{x}) = c_k\,/h^k + O(1), \text{ as } h \to 0,$$

as the contribution of the other segments of the polygon is $O(1)$. Thus

$$\Psi_k(\boldsymbol{x}) = \left[c_k\,/\varphi_k(\boldsymbol{x})\right]^{1/k} = h + O\left(h^{k+1}\right), \text{ as } h \to 0.$$

In particular, if $\boldsymbol{x}$ is an internal point of $\boldsymbol{ab}$, we have

$$\partial^s \Psi_k(\boldsymbol{x})/\,\partial\boldsymbol{n}^s = 0, \quad s = 2, 3, \ldots, k.$$

Now let us consider a domain D with a smooth boundary S oriented counterclockwise (see the middle image of Fig. 7 for the notations used). Consider a point $\boldsymbol{x} \in D$ on a distance $h \ll 1$ from S and assume that the curvature of S is positive in a vicinity of $\boldsymbol{x}$. Let $\boldsymbol{ab}$ be a circular arc osculating S at the point closest to $\boldsymbol{x}$ such that the segment $\boldsymbol{ab}$ is perpendicular to the direction from $\boldsymbol{x}$ to its closest neighbor on S, as seen in the middle image of Fig. 7. Let us also consider another circular arc $\boldsymbol{cd}$ such that it is situated inside D, $\boldsymbol{ab}$ and $\boldsymbol{cd}$ are collinear, and the direction from $\boldsymbol{x}$ to its closest neighbor on S is the bisector for $\boldsymbol{cd}$.

Now we approximate $\varphi_k(\boldsymbol{x})$ given by (3) by the sum of integrals of $1/\rho(\theta)^k$ over the circular arcs $\boldsymbol{ab}$ and $\boldsymbol{cd}$. Note that, as $\boldsymbol{x}$ approaches S, the osculating arc $\boldsymbol{ab}$ delivers a better and better local approximation of S and the leading term in asymptotics $\varphi_k(\boldsymbol{x})$, as $h \to 0$, is the same as that in the integral of $1/\rho(\theta)^k$ over the circular arc $\boldsymbol{ab}$.

Let R be the radius of the osculating circle. The law of cosines and simple algebraic manipulations yield

$$I_k(h) = \int_{-\pi/2}^{\pi/2} \frac{d\theta}{\rho(\theta)^k} = \int_{-\pi/2}^{\pi/2} \frac{d\theta}{\left[\sqrt{R^2 - (R-h)^2\sin^2\theta} - (R-h)\cos\theta\right]^k}$$
$$= \int_{-\pi/2}^{\pi/2} \left[\sqrt{R^2 - (R-h)^2\sin^2\theta} + (R-h)\cos\theta\right]^k \Big/ \left[2Rh - h^2\right]^k d\theta$$
$$= \frac{1}{h^k}\int_{-\pi/2}^{\pi/2} \cos^k\theta\,d\theta + \frac{k}{2R\,h^{k-1}}\int_{-\pi/2}^{\pi/2} \cos^{k-2}\theta\sin^2\theta\,d\theta + O\left(\frac{1}{h^{k-2}}\right)$$

which implies that

$$I_k(h) = c_k\,h^{-k} + d_k\,h^{1-k}/\,R + O\left(h^{2-k}\right), \text{ as } h \to 0. \tag{9}$$

$$\text{with} \quad c_k = \int_{-\pi/2}^{\pi/2} \cos^k \theta \, d\theta \quad \text{and} \quad d_k = c_{k-2}/\, 2.$$

The case of negative curvature (see the right image of Fig. 7) is considered similarly:

$$1 \Big/ \rho(\theta)^k = \left[(R+h)\cos\theta - \sqrt{R^2 - (R+h)^2 \sin^2\theta} \right]^{-k}$$
$$= \left[(R-h)\cos\theta + \sqrt{R^2 - (R+h)^2 \sin^2\theta} \right]^{k} \Big/ \left[2Rh + h^2 \right]^k.$$

The integration limits are $-\alpha$ and α, where 2α is the angle made by the two rays originated from $\boldsymbol{x}$ and tangent to the osculating circle, $\sin\alpha = R/(R+h)$. This leads to

$$I_k(h) = c_k \, h^{-k} - d_k \, h^{1-k} / \, R + O\left(h^{2-k}\right), \text{ as } h \to 0. \quad (10)$$

Asymptotics (9) and (10) suggest that the second term is proportional to the curvature of S at the point closest to $\boldsymbol{x}$.

In the nD case, for a single $(n-1)$-dimensional mesh tetrahedron (a mesh triangle in $3D$), we have

$$\varphi_k(\boldsymbol{x}) = \int \frac{d\Omega_y}{\rho^k} = \int \frac{h \, dS_y}{\rho^{k+n}}, \quad \rho = |\boldsymbol{x} - \boldsymbol{y}|.$$

So we arrive at a generalization of (8) for the multidimensional case

$$(k+n)\varphi_{k+2}(\boldsymbol{x}) = \frac{1}{h^2}\varphi_k(\boldsymbol{x}) - \frac{1}{h}\frac{\partial \varphi_k(\boldsymbol{x})}{\partial h}.$$

It is shown in [4] that $\varphi_1(\boldsymbol{x}) = v_{n-1}/\, h + O(1)$, as $h \to 0$, which justifies that $c_1 = v_{n-1}$ in (6).

The multidimensional case of smooth S is much more computationally demanding and can be analyzed by using osculating paraboloids for local approximations of S.

Proof of Proposition 3. Differentiating of (1) w.r.t $\boldsymbol{x}$ yields

$$\Delta\phi_k(\boldsymbol{x}) = k(k+n)\phi_{k+2}(\boldsymbol{x}).$$

For $k = 1$ and $\sigma(\boldsymbol{y}) \equiv 1$ this formula coincides with that obtained in [4]. Obviously $\phi_k(\boldsymbol{x})$ is positive if surface generalized-dipole density $\sigma(\boldsymbol{y})$ is positive. Assume that $\phi_k(\boldsymbol{x})$ has a local maximum at some point inside the domain bounded by S. Then $\Delta\phi_k(\boldsymbol{x}) \le 0$ at that point. We arrive at a contradiction which completes the proof.

References

[1] N. Ahuja and J.-H. Chuang. Shape representation using a generalized potential field model. *IEEE Transactions on Pattern Analysis and Machine Intelligence*, 19(2):169–176, 1997.

[2] A. Biswas and V. Shapiro. Approximate distance fields with non-vanishing gradients. *Graphical Models*, 66(3):133–159, 2004.

[3] A. Biswas, V. Shapiro, and I. Tsukanov. Heterogeneous material modeling with distance fields. *Comput. Aided Geom. Des.*, 21:215–242, 2004.

[4] S. Bruvoll and M. S. Floater. Transfinite mean value interpolation in general dimension. *J. Comp. Appl. Math.*, 233:1631–1639, 2010.

[5] M. Carley. Potential integrals on triangles. Technical Report arXiv1201.4938, January 2012.

[6] J.-H. Chuang, C.-H. Tsai, and M.-C. Ko. Skeletonization of three-dimensional object using generalized potential field. *IEEE Transactions on Pattern Analysis and Machine Intelligence*, 22(11):1241–1251, 2000.

[7] K. Crane, C. Weischedel, and M. Wardetzky. Geodesics in heat. Technical Report arXiv:1204.6216v1, April 2012.

[8] C. Dyken and M. S. Floater. Transfinite mean value interpolation. *Comp. Aided Geom. Design.*, 26:117–134, 2009.

[9] Z. Farbman, G. Hoffer, Y. Lipman, D. Cohen-Or, and D. Lischinski. Coordinates for instant image cloning. *ACM Trans. Graph.*, 28(3):67:1–67:9, 2009. ACM SIGGRAPH 2009.

[10] P.-A. Fayolle, A. Pasko, B. Schmitt, and N. Mirenkov. Constructive heterogeneous object modeling using signed approximate real distance functions. *ASME Journal of Computing and Information Science in Engineering*, 6(3):221–229, 2006.

[11] M. S. Floater. Mean value coordinates. *Computer Aided Geometric Design*, 20(1):19–27, 2003.

[12] M. Freytag, V. Shapiro, and I. Tsukanov. Finite element analysis in situ. *Finite Elem. Anal. Des.*, 47(9):957–972, 2011.

[13] A. Ghosh, C. S. Rapp, and R. A. Friesner. Generalized Born model based on a surface integral formulation. *J. Phys. Chem. B*, 102:10983–10990, 1998.

[14] K. S. Gurumoorthy, A. Rangarajan, and M. Sethi. Fast convolution-based methods for computing the signed distance function and its derivatives. Technical Report arXiv:1112.3010v1, December 2011.

[15] K. Hormann and M. S. Floater. Mean value coordinates for arbitrary planar polygons. *ACM Trans. Graph.*, 25(4):1424–1441, 2006.

[16] T. Ju, S. Schaefer, and J. Warren. Mean value coordinates for closed triangular meshes. *ACM Trans. Graph.*, 24(3):561–566, 2005. ACM SIGGRAPH 2005.

[17] L. V. Kantorovich. Some remarks on Ritz's method. *Trydy vysshego voenno-morskogo inzhenerno-stroitel'nogo uchilishcha*, (3), Leningrad, 1941. (Russian).

[18] L. V. Kantorovich and V. I. Krylov. *Approximate Methods of Higher Analysis.* Interscience Publishers, 1958. Chapter 4, § 2.

[19] Y. Liu. *Fast Multipole Boundary Element Method: Theory and Applications in Engineering.* Cambridge University Press, 2009.

[20] V. P. Maslov and M. V. Fedoryuk. Logarithmic asymptotic of rapidly decreasing solutions of Petrovskii hyperbolic equations. *Math. Notes*, 45:382–391, 1989.

[21] E. I. Ostrovskii. Exact asymptotics of Laplace integrals for nonsmooth functions. *Math. Notes*, 73:838–842, 2003.

[22] J. Peng. *Thick Surfaces: Interactive Modeling of Topologically Complex Geometric Details.* PhD, Department of Computer Science, New York University, 2004.

[23] J. Peng, D. Kristjansson, and D. Zorin. Interactive modeling of topologically complex geometric detail. *ACM Trans. Graph.*, 23:635–643, 2004. ACM SIGGRAPH 2004.

[24] A. Ricci. A constructive geometry for computer graphics. *The Computer Journal*, 16(2), 1973.

[25] A. N. Romanov, S. N. Jabin, Y. B. Martynov, A. V. Sulimov, F. V. Grigoriev, and V. B. Sulimov. Surface generalized Born method: A simple, fast, and precise implicit solvent model beyond the Coulomb approximation. *J. Phys. Chem. A*, 108(43):9323–9327, 2004.

[26] V. L. Rvachev. *Theory of R-functions and Some Applications.* Naukova Dumka, 1982. Russian.

[27] V. Shapiro. Semi-analytic geometry with R-functions. *Acta Numerica*, 16:239–303, 2007.

[28] R. Wong. *Asymptotic Approximations of Integrals.* SIAM, 2001.